

Preprocessing choices affect RNA velocity results for droplet scRNA-seq data

Charlotte Soneson^{1,2,*}, Avi Srivastava^{3,4}, Rob Patro⁵, Michael B Stadler^{1,2}

¹ Friedrich Miescher Institute for Biomedical Research, Basel, Switzerland

² SIB Swiss Institute of Bioinformatics, Basel, Switzerland

³ New York Genome Center, New York, USA

⁴ Center for Genomics and Systems Biology, New York University, New York, USA

⁵ Department of Computer Science, University of Maryland, College Park, MD, USA

* Correspondence to charlotte.soneson@fmi.ch

Keywords: scRNA-seq, RNA velocity, quantification

Abstract

Experimental single-cell approaches are becoming widely used for many purposes, including investigation of the dynamic behaviour of developing biological systems. Consequently, a large number of computational methods for extracting dynamic information from such data have been developed. One example is RNA velocity analysis, in which spliced and unspliced RNA abundances are jointly modeled in order to infer a 'direction of change' and thereby a future state for each cell in the gene expression space.

Naturally, the accuracy and interpretability of the inferred RNA velocities depend crucially on the correctness of the estimated abundances. Here, we systematically compare four widely used quantification tools, in total yielding twelve different quantification approaches, in terms of their estimates of spliced and unspliced RNA abundances in four experimental droplet scRNA-seq data sets. We show that there are substantial differences between the quantifications obtained from different tools, and identify typical genes for which such discrepancies are observed. We further show that these abundance differences propagate to the downstream analysis, and can have a large effect on estimated velocities as well as the biological interpretation.

Our results highlight that abundance quantification is a crucial aspect of the RNA velocity analysis workflow, and that both the definition of the genomic features of interest and the quantification algorithm itself require careful consideration.

30 Introduction

31 Single-cell RNA-seq (scRNA-seq) enables high-throughput profiling of gene expression on a transcriptome-
32 wide scale in individual cells. The increased resolution compared to bulk RNA-seq, where only average
33 expression profiles of populations of cells are obtained, provides vastly improved potential to study
34 a variety of biological questions. One such question concerns the dynamics of biological systems, re-
35 flected in, e.g., cellular differentiation and development. While such dynamical processes would ideally
36 be studied via repeated transcriptome-wide expression profiling of the same cells over time, this is not
37 possible with current scRNA-seq protocols. Existing analysis methods for so called *trajectory inference*
38 are instead applied to one or several snapshots of a population of cells, assumed to comprise all stages
39 of the trajectory of interest. Many computational methods for trajectory inference from scRNA-seq have
40 been presented in the literature (reviewed by Saelens et al. (2019)). These methods typically use the
41 similarity of the gene expression profiles between cells to construct a (possibly branching) path through
42 the observed set of cells, representing the trajectory of interest. Projecting the cells onto this path then
43 provides an ordering of the cells by so called pseudotime.

44 A different approach to the investigation of developmental processes in scRNA-seq data instead
45 exploits the underlying molecular dynamics. The feasibility of such an approach is based on the obser-
46 vation that, with several commonly used library preparation protocols, not only exonic, but also intronic
47 and exon/intron boundary-spanning reads are observed (La Manno et al. 2018), and the insight that con-
48 sidering these in combination with the exonic reads would allow for direct inference of developmental
49 relationships among cells. Similar observations, coupled with a simple differential equation model of
50 transcriptional dynamics, were previously used for investigation of pre-mRNA dynamics and transcrip-
51 tional and post-transcriptional regulation of gene expression in exon arrays (Zeisel et al. 2011) and bulk
52 RNA-seq (Gaidatzis et al. 2015), as well as estimation of transcription, processing and degradation rates
53 in bulk RNA-seq (Gray et al. 2014). For scRNA-seq, La Manno et al. (2018) used the differential equation
54 model of Zeisel et al. (2011), describing the rate of change of unspliced pre-mRNA as well as spliced
55 mRNA molecules, as a basis for their investigations. They defined the *RNA velocity* for a given gene in
56 a given cell, at a given time point, as the instantaneous rate of change of the spliced mRNA abundance.
57 Combining the RNA velocities with the estimated mRNA abundances enables reconstruction of the state
58 of each cell at a timepoint in the near future. With the increased popularity of RNA velocity applications
59 in scRNA-seq studies, several computational tools have been developed, both for the preprocessing of
60 the reads and for the RNA velocity estimation. The original *velocity* software (La Manno et al. 2018)
61 estimates velocities under a steady-state assumption, and provides both Python and R implementations.
62 More recently, Bergen et al. (2019) relaxed the steady-state assumption and considered the full dynam-
63 ical model, thereby enabling application of the RNA velocity framework to a broader set of biological
64 systems and states. The dynamical model is implemented in their *scVelo* Python package, which also
65 includes an efficient implementation of the steady-state model.

66 The input to both *velocity* and *scVelo* effectively consists of two gene-by-cell count matrices; one rep-
67 resenting mRNA ("spliced") abundances and one representing pre-mRNA ("unspliced") abundances. In
68 practice, these two types of abundances are typically represented by reads mapping to the exonic and
69 intronic regions of the genome, respectively. *Velocity* provides functions for parsing a BAM file of aligned
70 reads (obtained by other tools such as *CellRanger* (Zheng et al. 2017)) and generating these two count ma-
71 trices. Dedicated end-to-end functionality for estimation of spliced and unspliced abundances from raw

72 scRNA-seq reads are available within the *kallisto|bustools* software suite (Melsted, Ntranos, and Pachter
73 2019; Melsted et al. 2019) and in *STARsolo*, the single-cell mode of the *STAR* aligner (Dobin et al. 2013).
74 Furthermore, assuming a properly specified set of reference sequences, the required counts can also be
75 obtained using other general-purpose tools for quantification of droplet scRNA-seq data, such as *alevin*
76 (Srivastava et al. 2019a). To our knowledge, no critical evaluation of the differences between the count
77 matrices generated by these tools, and the effects on the downstream RNA velocity estimates, has been
78 performed to date. In this study, we therefore used four public experimental droplet scRNA-seq data
79 sets, generated with the 10x Genomics platform, to compare spliced and unspliced abundance estimates
80 obtained by *velocity*, *kallisto|bustools*, *STARsolo* and *alevin*. Including alternative index definitions and
81 parameter settings, we analyzed each of the four experimental data sets with a total of up to twelve dif-
82 ferent quantification approaches (tool/parameter/index combinations). We illustrate that the estimates
83 of spliced and unspliced abundances can be strongly affected by the choice of tool, as well as by the
84 delineation of exonic and intronic regions; in particular, how genomic regions that are exonic in some
85 annotated transcript isoforms and intronic in others are treated. Moreover, we show that abundance esti-
86 mation is a critical step of the analysis workflow and that differences at this stage can have considerable
87 effects on both the RNA velocity estimates and subsequent biological interpretation.

88 **Methods**

89 **Data**

90 In this study, we used four public single-cell RNA-seq data sets, generated by different laboratories
91 using popular droplet-based protocols from 10x Genomics. Three of the four data sets (Pancreas, Dentate
92 gyrus and Spermatogenesis) comprise cells from dynamically developing systems, while the fourth (PFC)
93 contains differentiated cells from adult mouse brain and was chosen as a negative control data set,
94 assumed to not harbor a strong dynamic signal.

- 95 • The Pancreas data set (Bastidas-Ponce et al. 2019) stems from a study of endocrine development
96 in mouse, and was acquired with the 10x Genomics Chromium platform, using v2 chemistry. We
97 downloaded the FASTQ files containing the reads from the cells at stage E15.5 from the Gene
98 Expression Omnibus, accession number GSE132188. The RNA read length is 151 nt. A subset of
99 this data set was used for illustration by Bergen et al. (2019), and is included as an example data
100 set in the *scVelo* package. After the respective quantifications, we retained only the cells that are
101 also included in the *scVelo* example data set, from which we also retrieved cell type labels. The final
102 processed data set used for our analyses contains 3,696 cells.
- 103 • The Dentate gyrus data set (Hochgerner et al. 2018) considers the developing mouse dentate gyrus,
104 and was acquired with 10x Genomics v1 chemistry. The individual FASTQ files for cells from P12
105 and P35 were downloaded from the Gene Expression Omnibus, accession number GSE95315, and
106 the reads from each time point were combined in a single pair of FASTQ files, with cell barcodes
107 and UMI sequences in one file and the read sequence in the other. The RNA read length is 98 nt.
108 Similarly to the Pancreas data set, the Dentate gyrus data set is also available as an example data
109 set in *scVelo*, and was used for illustration by Bergen et al. (2019). Only cells that were also studied
110 in the *scVelo* paper were retained for our analysis, and cell type labels were obtained from the

111 *scVelo* example data set. *CellRanger* and *velocity* were not run on this data set since the downloaded
112 FASTQ files were not in the format expected by these tools. The final processed data set used for
113 our analyses contains 2,914 cells.

- 114 • The Spermatogenesis data set (Hermann et al. 2018) consists of steady-state spermatogenic cells
115 from an adult mouse, and was processed with 10x Genomics Chromium v2 chemistry. The submit-
116 ted BAM file was downloaded from the Gene Expression Omnibus, accession number GSE109033
117 (sample accession number GSM2928341), and converted to FASTQ format using the *bamtofastq* util-
118 ity (v1.1.2) from 10x Genomics (<https://support.10xgenomics.com/docs/bamtofastq>). The RNA
119 read length is 100 nt. Cell type labels were obtained from the corresponding loupe browser file pro-
120 vided by the authors, downloaded from <https://data.mendeley.com/datasets/kxd5f8vpt4/1>.
121 Only cells that were also included in this file were retained for further analysis after quantification.
122 The final processed data set used for our analyses contains 1,829 cells.
- 123 • The PFC data set (Bhattacharjee et al. 2019) consists of cells from the prefrontal cortex of an adult
124 mouse, and was generated using 10x Genomics Chromium v2 chemistry. Since only limited dy-
125 namics is expected in this data set, it is used here as a negative control. The submitted BAM
126 file was downloaded from the Gene Expression Omnibus, accession number GSE124952 (sample
127 accession GSM3559979), and converted to FASTQ format using the *bamtofastq* utility (v1.1.2) from
128 10x Genomics (<https://support.10xgenomics.com/docs/bamtofastq>). The RNA read length is
129 98 nt. Only cells annotated to ‘PFC sample 2’ were used, and cell type labels assigned by the data
130 generators were obtained from the GEO record metadata. The final processed data set used for our
131 analyses contains 1,267 cells.

132 Feature sequence extraction

133 All analyses are based on reference files from Gencode, mouse release M21 (Frankish et al. 2019). The
134 desired output from each quantification method is a pair of count matrices; one containing ‘spliced’ or
135 ‘exonic’ counts, and the other containing ‘unspliced’ or ‘intronic’ counts for each gene in each cell. For
136 simplicity, in the remainder of this paper, the terms ‘spliced’ and ‘exonic’ will be used interchangeably to
137 refer to the counts representing the processed mRNA abundances, and ‘unspliced’ and ‘intronic’ counts
138 will similarly refer to the counts representing the unprocessed pre-mRNA abundances.

139 To enable this type of quantification with *alevin* and *kallisto* | *bustools* (as opposed to the more standard,
140 gene-level expression quantification), the Gencode reference files were processed as follows (also summa-
141 rized in Table 1). First, we used the *BUSpaRse* R/Bioconductor package v1.0.0 (Moses and Pachter 2019)
142 to extract transcript and intron sequences from the genome sequence and the Gencode annotation GTF
143 file. While the definition of the transcripts is unambiguous, the *BUSpaRse* package supports two ways
144 of defining the introns (see Fig. S1 for a schematic). The ‘separate’ approach considers each transcript
145 separately when extracting the intronic regions (and thus, an intron can overlap with an exonic region
146 of an alternate transcript), while the ‘collapse’ approach first collapses the isoforms of a gene (taking the
147 union of all the exonic regions) before defining the introns as any regions of the gene locus that are not
148 exonic in any of the annotated transcript isoforms of the gene. In effect, the ‘separate’ approach thus
149 considers exonic and intronic regions on an equal footing, while the ‘collapse’ approach represents a
150 prior belief that an ambiguous read is more likely to come from an exon than from an intron. A flanking

151 sequence of length $L - 1$ (where L is the RNA read length of the respective study) is added on each side
152 of each intron to account for reads mapping across exon/intron boundaries. For comparison, we also
153 reimplemented the extraction of transcript and intron sequences (for both the ‘separate’ and ‘collapse’
154 approaches) directly using functions from the *GenomicFeatures* and *BSgenome* R/Bioconductor packages
155 (Pagès 2019; Lawrence et al. 2013). Code used to extract the features has been included in the *eisaR*
156 package (<https://github.com/fmicompbio/eisaR>), from v0.9, for convenience. In each case, the ex-
157 tracted transcript and intron sequences were written to a joint FASTA file, summarized in Table 1. Upon
158 comparison of the two implementations, we noticed that the current release version (v1.0.0) of *BUSpaRse*
159 returned erroneous feature sequences for multi-exonic transcripts on the negative strand (Fig. S2). For
160 this reason, the features extracted by *BUSpaRse* were not used for further analyses.

FASTA file name	Sequence extraction	Description
BUSpaRse-separate	<i>BUSpaRse</i>	Introns extracted separately from each transcript isoform
BUSpaRse-collapse	<i>BUSpaRse</i>	Introns extracted after collapsing all transcripts of a gene
eisaR-separate	<i>eisaR</i>	Introns extracted separately from each transcript isoform
eisaR-collapse	<i>eisaR</i>	Introns extracted after collapsing all transcripts of a gene

Table 1: Summary of reference FASTA files containing exonic and intronic sequences. Only files generated by *eisaR* were used for creation of quantification indices.

161 Reference index generation

162 The combined transcript and intron FASTA files were used to build the following quantification indices
163 (summarized in Table 2):

- 164 • a joint transcript and intron index for *Salmon* (v1.0.0) (Patro et al. 2017)
- 165 • an index for *Salmon*, considering the transcripts as the features of interest and providing the introns
166 as decoy sequences (Srivastava et al. 2019b)
- 167 • an index for *Salmon*, considering the introns as the features of interest and providing the transcripts
168 as decoy sequences
- 169 • a joint transcript and intron index for *kallisto* (v0.46.0) (Bray et al. 2016)

170 In addition to the indices based on transcripts and introns, we built one *Salmon* index from the
171 original Gencode FASTA file with the annotated transcripts, and one *Salmon* index from a FASTA file
172 combining the annotated transcripts and fully unspliced versions of all transcripts. For all *Salmon* in-
173 dices, the complete genome sequence was provided as a decoy sequence (Srivastava et al. 2019b), with
174 the aim to exclude reads coming from intergenic regions of the genome. Across data sets and reference

175 specifications, this excluded between 1 and 2.5% of the reads from the quantification. For the quantifica-
 176 tion based on spliced-only transcripts, in which the genome decoy would also capture unambiguously
 177 intronic reads, this number was between 2 and 10%. Finally, we built an index for *CellRanger* (v3.0.2)
 178 (Zheng et al. 2017) and one for *STAR* (v2.7.3a) (Dobin et al. 2013) based on the reference genome and
 179 GTF file from Gencode. The splice junction database overhang in the *STAR* index was set to 150nt, which
 180 is at least as long as the read length minus one for all data sets considered here.

Index type	Index building	Input reference files (Table 1)	Target sequences	Decoy sequences
salmon-joint	<i>Salmon</i>	eisaR-separate, eisaR-collapse	spliced transcripts and introns	genome
salmon-spliced	<i>Salmon</i>	transcriptome	spliced transcripts	genome
salmon- spliced- unspliced	<i>Salmon</i>	transcriptome + unspliced transcripts	spliced and unspliced transcripts	genome
salmon- spliced-decoy	<i>Salmon</i>	eisaR-separate, eisaR-collapse	spliced transcripts	introns + genome
salmon- introns-decoy	<i>Salmon</i>	eisaR-separate, eisaR-collapse	introns	spliced transcripts + genome
kallisto-joint	<i>kallisto</i>	eisaR-separate, eisaR-collapse	spliced transcripts and introns	N/A
cellranger	<i>CellRanger</i>	genome and GTF file	whole genome	N/A
star	<i>STAR</i>	genome and GTF file	whole genome	N/A

Table 2: Summary of reference indices. The full index name is constructed by concatenating the index type to the FASTA file name, e.g. salmon-joint-eisaR-separate refers to the salmon-joint index built for the sequences in the eisaR-separate FASTA file.

181 To investigate the effect of the choice of flank length in the intron definition, we further built *Salmon*
 182 indices (using the 'separate' intron definition) with flank lengths equal to the read length minus 21bp,
 183 and the read length minus 41bp. We also built an index for *kallisto* | *bustools* using the *kb-python* wrapper
 184 (Bray et al. 2016; Melsted et al. 2019), which uses the 'separate' intron definition and sets the flank length
 185 to 30 bp.

186 Sequence uniqueness estimation

187 Finally, to aid in the interpretation, we estimated the sequence uniqueness for each gene, relative to all
 188 other genes, separately for each FASTA file generated as described above (Table 1). The gene uniqueness
 189 was defined as the fraction of unique k-mers in the gene, that is, the fraction of the constituent k-mers
 190 that are not found in any other gene. For each data set, the k-mer length was set to be equal to the RNA
 191 read length minus 1. The sequence uniqueness for a gene was calculated in two different ways. In each
 192 case, the full FASTA file with transcript and intron sequences was used as input. First, we estimated

193 separate uniqueness values for the exonic and intronic parts of a gene, by assigning the transcripts and
194 introns of a gene to distinct gene IDs in the uniqueness calculations. With this approach, k-mers that are
195 exonic in one transcript and intronic in another (even if these are isoforms of the same gene) are classified
196 as non-unique, and thus the uniqueness score of an exon sharing some of its sequence with an intron
197 of another transcript from the same gene is reduced. Second, we estimated an overall gene uniqueness,
198 by again considering all (exonic and intronic) sequences, but not penalizing shared sequence between
199 introns and exons of the same gene.

200 **Quantification**

201 **alevin**

202 For each of the *Salmon* indices described above, we ran *alevin* (v1.0.0) (Srivastava et al. 2019a) to esti-
203 mate exonic and intronic abundances for each annotated gene. It is worth noting that for abundances
204 obtained with the salmon-spliced-unspliced index, ‘exonic’ and ‘intronic’ abundances refer directly to
205 spliced mRNA and unspliced pre-mRNA abundance estimates, respectively, while for all other indices,
206 ‘exonic’ abundances refer to exonic regions and ‘intronic’ abundances to intronic regions. This affects, for
207 example, how reads aligning completely within an exon are used in the quantification: For the salmon-
208 spliced-unspliced index, such a read could stem from either the spliced or the unspliced transcript (since
209 also the latter contains the exons) and could contribute to the abundance of either (or both) of them,
210 while with the other indices, it will be considered ‘exonic’.

211 For the *alevin* quantifications, the transcripts and introns (or unspliced transcripts) from the same
212 gene were manually annotated with different gene IDs, in order to obtain separate exonic and intronic
213 gene-level abundances despite estimating them jointly. For the indices with decoys, the exonic gene
214 counts were defined as the counts obtained when quantifying against the transcript index (with introns
215 as decoys) and the intronic gene counts were similarly obtained by quantifying against the intron index
216 (with transcripts as decoys). Hence, for these approaches, it is possible for a read that maps equally well
217 to an exonic and an intronic sequence to be included in both the exonic and the intronic count matrices,
218 and thus be counted twice.

219 **kallisto | bustools**

220 For each of the *kallisto* indices, we applied *kallisto | bustools* (v0.46.0) (Melsted, Ntranos, and Pachter 2019;
221 Melsted et al. 2019) to generate a BUS file. Barcodes were corrected using the list of available cell
222 barcodes from 10x Genomics for the appropriate chemistry version, and the BUS file was sorted using
223 *kallisto | bustools*. Next, the BUS file was subset with the capture command of *kallisto | bustools* to generate
224 separate BUS files to be used for the quantification of exonic and intronic features, respectively. The gene-
225 level exonic and intronic counts were subsequently obtained using the count command. The capture was
226 performed using two different approaches:

- 227 • ‘include’, where the features of interest for the quantification at hand are provided to *kallisto | bustools*.
228 In other words, the transcript IDs are provided as the `-c` argument to quantify the exonic abun-
229 dances, and the intron IDs are provided to quantify the intronic abundances. In practice, this
230 means that reads in equivalence classes containing at least one transcript are retained for the ex-
231 onic quantification, and reads in equivalence classes containing at least one intron are retained for

232 the intronic quantification. Hence, equivalence classes containing both exonic and intronic features
233 will be provided to both the exonic and intronic quantification steps.

234 • ‘exclude’, where the features that are not of interest for the quantification at hand are provided
235 to *kallisto|bustools*, and subsequently excluded. In other words, intron IDs are provided as the `-c`
236 argument to quantify the exonic abundances, and the transcript IDs are provided to quantify the
237 intronic abundances, and in addition the `-x` flag is used to indicate that the provided IDs represent
238 sequences to be excluded. In practice, this means that only reads in equivalence classes that don’t
239 contain *any* introns will be retained for the exonic quantification, and only reads in equivalence
240 classes that don’t contain any transcripts will be retained for the intronic quantification. Hence,
241 equivalence classes containing both exonic and intronic features will be excluded in both steps.

242 In addition to the manual application of *kallisto|bustools* as described above, we applied the *kb-*
243 *python* wrapper for quantification based on the corresponding index. With its default settings, it calls
244 *kallisto|bustools* with the ‘exclude’ capture approach.

245 **Velocity and STARsolo**

246 *CellRanger* (v3.0.2) (Zheng et al. 2017) and *velocity* (v0.17) (La Manno et al. 2018) were run with default
247 settings to generate exonic and intronic counts based on the *CellRanger* index. *STARsolo* (v2.7.3a) (Dobin
248 et al. 2013) was run using the *STAR* index, specifying the `SOLofeatures` argument to generate ‘Velocity’
249 (exonic and intronic), ‘Gene’ (regular exonic gene expression) and ‘GeneFull’ (reads with any overlap
250 with the gene locus) counts. Based on these count matrices, we obtained exonic and intronic count
251 matrices in two different ways. First, we directly used the ‘Velocity’ count matrices as exonic and intronic
252 counts (below referred to as *starsolo*). Second, we used the ‘Gene’ count matrix as the exonic counts, and
253 the difference between the ‘GeneFull’ and ‘Gene’ counts as the intronic counts (below referred to as
254 *starsolo_diff*). For genes where the ‘Gene’ counts were higher than the ‘GeneFull’ counts, the intronic
255 count was set to zero. This can happen, for example, for a gene located in the intron of another gene.
256 In the ‘GeneFull’ quantification, reads mapping to such a gene are considered ambiguous and therefore
257 discarded. However, they may be assigned in the ‘Gene’ quantification, if they are compatible with the
258 annotated gene model. An overview of the evaluated quantification approaches is provided in Table 3.

259 **Cell filtering and data processing**

260 For each quantification, we generated a `SingleCellExperiment` object (Lun and Risso 2019) containing
261 the exonic and intronic counts. Only cells and genes included by all methods were retained for further
262 analysis. For the Pancreas and Dentate gyrus data sets, we further subset the objects to only the cells
263 analyzed by Bergen et al. (2019), for the PFC data we kept only cells annotated to PFC sample 2, and for
264 the Spermatogenesis data set only cells with an assigned cell type label provided by the data generators
265 were retained. For visualization purposes, we calculated a single low-dimensional representation based
266 on the *alevin* quantification of only the spliced mRNAs (using the original transcriptome FASTA file
267 from Gencode). After normalization with *scater* v1.14.6 (McCarthy et al. 2017), using the library sizes as
268 size factors, we extracted 30 principal components from the log-transformed normalized count values.
269 The *scater* package was then used to apply UMAP (McInnes, Healy, and Melville 2018) with default

Method ID	Quant method	Index	Exonic/intronic quantification	Capture type
<i>alevin_coll_gtr</i>	<i>alevin</i>	salmon-joint-eisaR-collapse	joint	N/A
<i>alevin_coll_decoy_gtr</i>	<i>alevin</i>	exonic: salmon-spliced-decoy-eisaR-collapse, intronic: salmon-introns-decoy-eisaR-collapse	separate	N/A
<i>alevin_sep_gtr</i>	<i>alevin</i>	salmon-joint-eisaR-separate	joint	N/A
<i>alevin_sep_decoy_gtr</i>	<i>alevin</i>	exonic: salmon-spliced-decoy-eisaR-separate, intronic: salmon-introns-decoy-eisaR-separate	separate	N/A
<i>alevin_spliced_unspliced_gtr</i>	<i>alevin</i>	salmon-spliced-unspliced	joint	N/A
<i>kallisto bus_coll_excl</i>	<i>kallisto bustools</i>	kallisto-joint-eisaR-collapse	separate	exclude
<i>kallisto bus_coll_incl</i>	<i>kallisto bustools</i>	kallisto-joint-eisaR-collapse	separate	include
<i>kallisto bus_sep_excl</i>	<i>kallisto bustools</i>	kallisto-joint-eisaR-separate	separate	exclude
<i>kallisto bus_sep_incl</i>	<i>kallisto bustools</i>	kallisto-joint-eisaR-separate	separate	include
<i>starsolo</i>	<i>STAR</i>	star	joint	N/A
<i>starsolo_diff</i>	<i>STAR</i>	star	exonic: Gene, intronic: GeneFull - Gene	N/A
<i>velocyto</i>	<i>velocyto</i>	CellRanger	joint	N/A

Table 3: Summary of quantification approaches. In addition to the strategies included in this table, we applied *alevin_sep_gtr* after using different flank length when defining the intronic reference sequences, *alevin_sep_gtr* in unstranded mode, and the *kb-python* wrapper around *kallisto|bustools*. The effects of these modifications are evaluated in Fig. S3.

270 parameters to the PCA output to obtain a two-dimensional representation that was used for visualization
271 of estimated velocities.

272 Visualization

273 In order to visualize the coverage pattern of reads within genomic regions, we subset the BAM file
274 generated by *CellRanger* to only the reads assigned to the retained cell barcodes, using the *subset_bam*
275 tool v1.0 from 10x Genomics (<https://github.com/10XGenomics/subset-bam>). Next, we used *BEDTools*
276 v2.27.1 (Quinlan and Hall 2010) to calculate the coverage along the genome, separately for reads on the
277 positive and negative strand. The *bedGraphToBigWig* script from Kent Tools v20190212 (Kent et al. 2010)
278 was used to convert the resulting bedGraph file to bigwig format.

279 Coverage patterns, together with annotated gene models, were visualized using the *Gviz* R/Bioconductor
280 package v1.30.0 (Hahne and Ivanek 2016). In these figures, the annotated gene models are visualized by
281 their genomic coordinates, together with coverage tracks of reads aligned to the positive and negative
282 strand of the genome. The alignments are aggregated across all the retained cells in the data set. All
283 alignments contained in the BAM file are included; hence, multimapping reads are represented in all the
284 reported mapping locations. Moreover, no UMI deduplication is performed and thus the number of reads
285 reported in the coverage tracks are often higher than the total UMI count returned by any of the counting
286 methods. It is also important to note that while the gene models and coverage tracks are represented
287 with respect to a genomic reference for ease of interpretation, both *alevin* and *kallisto | bustools* perform the
288 quantification based on mapping to transcriptomic features, not alignment to the genome. Thus, these
289 plots are not intended to provide an exact correspondence between mapped reads and estimated UMI
290 counts, but rather serve as illustrations to aid in the understanding of the causes of differences between
291 the counts from the various methods.

292 RNA velocity estimation

293 SingleCellExperiment objects with exonic and intronic gene-level UMI counts were converted to Ann-
294 Data objects (Wolf, Angerer, and Theis 2018) using the *anndata2ri* package v1.0 ([https://github.com/](https://github.com/theislab/anndata2ri)
295 [theislab/anndata2ri](https://github.com/theislab/anndata2ri)). The *scVelo* package v0.1.24 (Bergen et al. 2019) was then used to normalize the
296 counts and select the 2,000 most highly variable genes separately for each quantification approach, after
297 excluding all genes with less than 20 assigned reads across the exonic and intronic components (only
298 summing across cells with nonzero exonic and intronic count). Note that by default, *scVelo* selects highly
299 variable genes based on the spliced counts only. RNA velocity estimates were obtained using the dy-
300 namical model implemented in *scVelo*. For comparison, we also performed downstream analysis and
301 visualization of the RNA velocity using only the genes that were selected (and for which *scVelo* returned
302 a finite velocity value) by *scVelo* with all the quantification approaches.

303 The *scVelo* analysis returns a gene-by-cell matrix of estimated velocities, as well as corresponding
304 matrices of normalized (spliced and unspliced) abundances. Based on these matrices, we estimated
305 both gene- and cell-wise Spearman correlations between the different types of abundances, as well as
306 between the abundances and the velocity estimates. It is worth noting that the velocity calculations are
307 performed separately for each input gene, and the resulting values are therefore independent of which
308 other genes are included in the data set (under the assumption that the normalized abundance values
309 stay unchanged).

310 Based on the estimated velocity vectors and the differences between the expression profiles of differ-
311 ent cells, *scVelo* calculates a cosine correlation (π_{ij}) for each pair of 'neighboring' cells. A high value of

312 π_{ij} indicates that the velocity vector of cell i points in the direction from cell i to cell j in gene expression
313 space. Conversely, if, for a given i , π_{ij} is small for all j , the velocity vector of cell i does not point in the
314 direction of any other cell in its neighborhood. With this in mind, we calculate $\max_j \pi_{ij}$ for each cell i
315 and use this as a proxy for the presence of systematic dynamics in a data set. For each cell, *scVelo* further
316 provides an estimate of the velocity confidence (representing the average correlation of the velocity vec-
317 tor of the cell and those of its neighbors), and an estimated shared (across genes) latent time. The latter
318 was used to contrast the negative control data with the other three data sets, based on the assumption
319 that for a data set without continuous dynamics, the latent time estimates for cells of the same cell type
320 would be more similar to each other than in a data set with a continuous dynamic signal.

321 Low-dimensional embedding of velocities

All velocity estimates were embedded into the same low-dimensional representation, calculated from the spliced-only abundance quantification by *alevin* as described above. The embedded velocity vector for cell i , calculated by *scVelo*, is given by

$$\tilde{v}_i = \sum_{j \neq i} \left(\tilde{\pi}_{ij} - \frac{1}{n} \right) \tilde{\delta}_{ij}$$

where $\tilde{\pi}_{ij}$ is the transition probability from cell i to cell j (derived from the cosine correlation π_{ij}), n is the number of cells, and

$$\tilde{\delta}_{ij} = \frac{\tilde{s}_j - \tilde{s}_i}{\|\tilde{s}_j - \tilde{s}_i\|}$$

is the normalized difference of the coordinates of cells i and j in the low-dimensional embedding. The fact that $\tilde{\delta}_{ij}$ is normalized implies that the length of \tilde{v}_i indicates to what extent the cells to which cell i has high transition probabilities are all located in the same direction from cell i in the low-dimensional representation. It further implies that the embedded velocities are potentially more comparable across methods than the original velocity vectors, since the magnitudes of the latter depend on the normalized abundance levels of the genes, and since the velocity vectors will only be directly comparable between methods if they are based on the same set of input genes. In order to compare the velocity embeddings across methods, we calculate a concordance score for each cell. The score for cell i is defined as the ratio between the length of the sum of the embedded velocity vectors for cell i across all quantification methods, and the sum of the lengths of the individual embedded velocity vectors. In other words, the score for cell i is given by

$$c_i = \frac{\|\sum_m \tilde{v}_i^{(m)}\|}{\sum_m \|\tilde{v}_i^{(m)}\|}$$

322 where the sum is taken over all methods m , and $\tilde{v}_i^{(m)}$ is the embedded velocity vector for cell i with
323 method m . If all embedded velocity vectors for cell i point in the same direction in the low-dimensional
324 representation, this ratio will be close to 1, while if there is less concordance between the different
325 quantification methods, the ratio will be lower than 1.

326 Results

327 The total UMI count varies between methods

328 With the aim of characterizing global differences between the counting methods, we first directly com-
329 pared the total UMI count assigned to exonic and intronic targets by each of the methods. We added up
330 the counts across all cells, either across all genes or within gene subsets stratified by sequence uniqueness
331 (Fig. 1, Pancreas data, similar values were obtained for the other three data sets). There are consider-
332 able differences in the assigned UMI counts between the methods. Moreover, these differences are not
333 confined to a small number of susceptible genes, but can be seen across a large fraction of the expressed
334 genes (Fig. S4).

335 Overall, *starsolo_diff* and the *alevin*-based quantification approaches based on transcript/intron an-
336 notations gave the highest total UMI counts, mainly driven by higher counts for the exonic targets. As
337 shown in Fig. 1, this is predominantly due to the assignment of reads to genes with a low fraction of
338 unique k-mers. This is in contrast to *kallisto|bustools*, *velocity* and *starsolo*, which by default exclude
339 ambiguous reads that map to multiple genes from the quantification.

340 *Velocity* and *starsolo_diff* gave the highest UMI counts for genes whose transcripts are all shorter than
341 the read length (genes in the 'NA' category in Fig. 1, for which no uniqueness could be calculated since
342 all transcripts were shorter than the employed k-mer length). However, *velocity* considered most of these
343 reads to be exonic, while *starsolo_diff* assigned them to the intronic features. This behaviour of *starsolo_diff*
344 is likely due to the generation of the intronic counts by subtraction of the exonic count from the full gene
345 locus count. A read which partly overlaps the gene locus but is not consistent with the annotated gene
346 model would be included in the 'GeneFull' count but not in the 'Gene' count, and thus considered an
347 intronic read, regardless of whether or not the gene actually contains any introns. Similarly, *starsolo_diff*
348 assigned higher counts than both *velocity* and the default 'Velocity' counting of *starsolo*, for both exonic
349 and intronic features.

350 As expected, the *alevin*-based approaches where exonic and intronic features are quantified separately,
351 as well as the 'include' capture mode of the *kallisto|bustools* approaches, tend to give higher total UMI
352 count than quantifying exonic and intronic features jointly with *alevin* or running *kallisto|bustools* in
353 'exclude' capture mode, especially for the 'separate' intron definition. This is likely due to double-
354 counting of some reads that map equally well to an exon and an intron. The difference between the
355 'include' and 'exclude' capture approaches is smaller for the 'collapse' annotation, since in that case,
356 no genomic regions are annotated as both intronic and exonic for the same gene. The same is true
357 for the difference between the *alevin* quantifications employing joint and separate quantification. It is
358 worth noting that the length of the flanking region chosen when constructing the intronic features for
359 the quantification also influences the counts (Fig. S3). A shorter flank length typically leads to a lower
360 unspliced count, since a larger fraction of the read must overlap the intron for the read to be considered
361 potentially intronic.

362 In addition to the absolute counts, also the fraction of UMIs assigned to unspliced targets varies
363 between methods, with the largest fraction of intronic counts obtained by *alevin_spliced_unspliced*. This
364 was expected, given that for this method, the 'intronic' features are the full pre-mRNA molecules and
365 thus contain both exonic and intronic sequences. Hence, also reads falling in exons may be assigned to
366 the unspliced features.

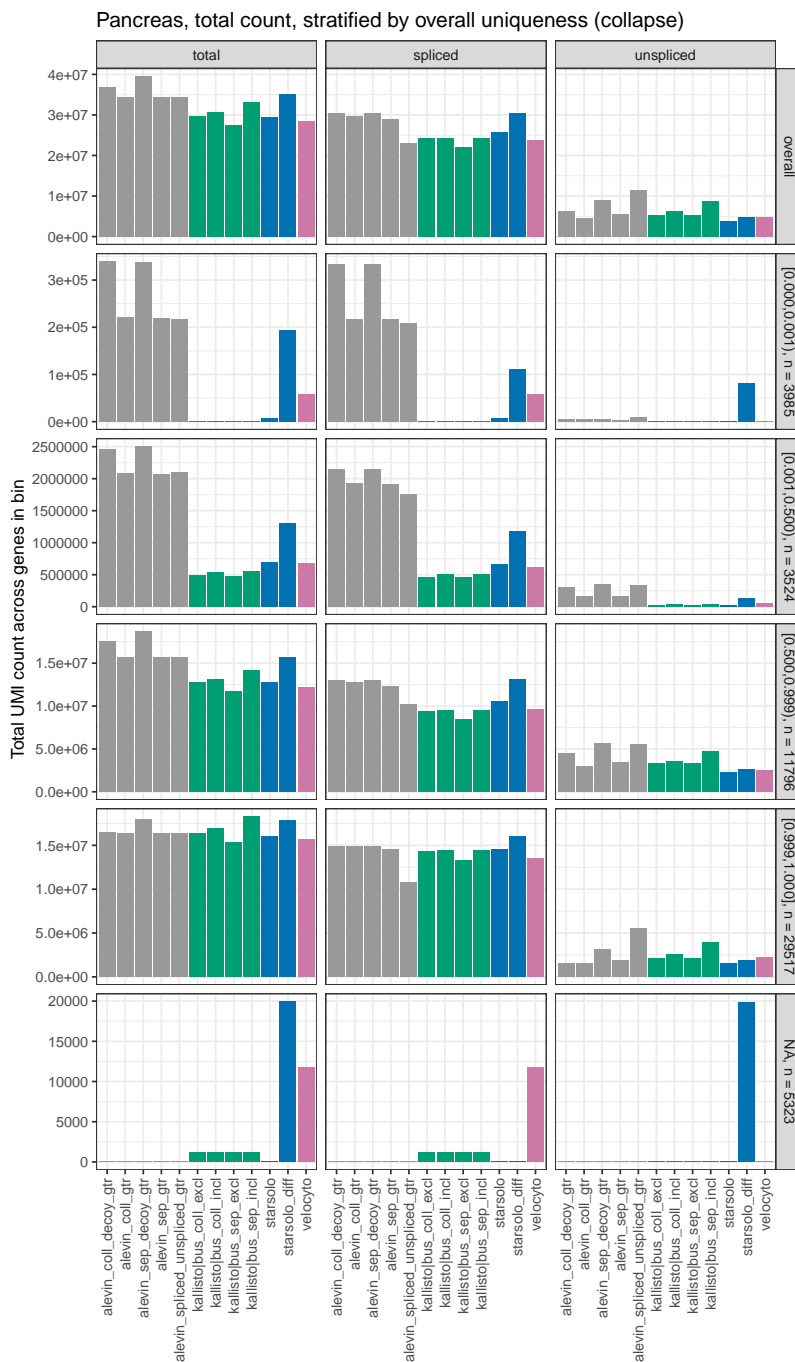


Figure 1: Total UMI count across genes and cells. The bars correspond to the total UMI count, and the split of these into counts for exonic and intronic targets, for each quantification method in the Pancreas data set. Similar patterns were seen in the other three data sets. In addition to the overall count (top row), the figure shows the total count after stratifying genes by the overall fraction of unique k-mers (using the 'collapse' annotation), indicated in the vertical panel headers together with the number of genes in the category. The genes for which no uniqueness information could be calculated (the 'NA' category) are those for which all transcripts are shorter than the chosen k-mer length (which was set to the read length minus one; here 150nt).

367 Individual genes exemplify methodological differences

368 Next, we aimed to find individual genes whose count patterns exemplify the main methodological dif-
369 ferences among the counting strategies. First, we restricted the set of genes to those that were selected as
370 highly variable by *scVelo*, and thus used for velocity estimation, for at least one counting method. Notably,
371 while a large fraction of these genes were selected across all quantification methods, there were non-
372 negligible differences between the sets of selected genes (Fig. S5). In particular, *alevin_spliced_unspliced*
373 gave the largest number of unique highly variable genes, followed by the *starsolo* variants and *velocyto*
374 depending on the data set. For each of the retained genes, we calculated the fraction of the total counts
375 that were assigned to unspliced features (summarized across all cells). Next, we calculated the standard
376 deviation, across the quantification methods, of these intronic count fractions and selected the top 10%
377 of the genes based on this measure. These genes were partitioned into 10 clusters based on the Pearson
378 correlation dissimilarity ($\sqrt{2(1-\rho)}$ where ρ is the Pearson correlation) between the fractions of intron-
379 assigned counts across methods, using hierarchical clustering with complete linkage (Fig. 2). The gene
380 clusters reveal typical cases where the methods yield different exonic and/or intronic counts. Repre-
381 sentative genes for each cluster, selected among the genes with the highest correlation with the cluster
382 centroid, are discussed below and illustrated in Figs. S6-S7.

383 **Genes with ambiguous regions** (clusters 4, 5, 7, exemplified by *Tspan3*, *Sirt3* and *Ssr1* in Fig. S6).
384 For genes in which many of the base positions are annotated to both exons and introns (in different
385 isoforms), the choice of how to define introns ('separate' vs 'collapse' approaches) has a major effect on
386 the quantifications. If exons are collapsed before the introns are defined, reads falling in ambiguous
387 regions are considered exonic, leading to a higher exonic and a lower intronic count than with the
388 'separate' intron definition. This effect can be seen in approximately half of the genes with the highest
389 variability in the fraction of unspliced counts (Fig. 2), and manifests itself via a low fraction of unspliced
390 reads for the methods based on annotations obtained with the 'collapse' intron definition approach. Also
391 *starsolo_diff* falls in this category, since the intronic regions are not considered when the exonic counts
392 are estimated (via the 'Gene' count), and thus any read that is compatible with at least one transcript
393 model is considered exonic.

394 With the 'separate' intron definition, running *alevin* with decoys or *kallisto|bustools* with the 'include'
395 capture double-counts many reads falling completely in ambiguous regions, giving high values of both
396 exonic and intronic counts. Conversely, running *kallisto|bustools* with 'exclude' capture discards many
397 reads in ambiguous regions, since they will typically be assigned to equivalence classes containing both
398 exonic and intronic targets, and this counting strategy therefore often returns low counts for both types
399 of features. While these effects can be seen in the absolute counts, they do not necessarily affect the ratio
400 of spliced and unspliced counts (Fig. S6).

401 For genes with many ambiguous regions, *velocyto* often returns a relatively low number of spliced
402 counts, and consequently a large fraction of unspliced counts (clusters 4, 7). This follows from the
403 default 'permissive' counting logic where, essentially, a read contributes to the spliced count only if it
404 is consistent with the exonic region of a transcript model, but does not map to an intronic region or an
405 exon/intron boundary of any other transcript model. Also *starsolo* often assigns a low total count for this
406 group of genes.

407 **Genes overlapping (introns of) other genes** (clusters 1, 2, 3, 6, 10, exemplified by *Chkb*, *Gm21983*,
408 *Rassf1*, *Cnot6* and *Tmem120b* in Fig. S7). Overlaps between genes can take many different shapes; exons

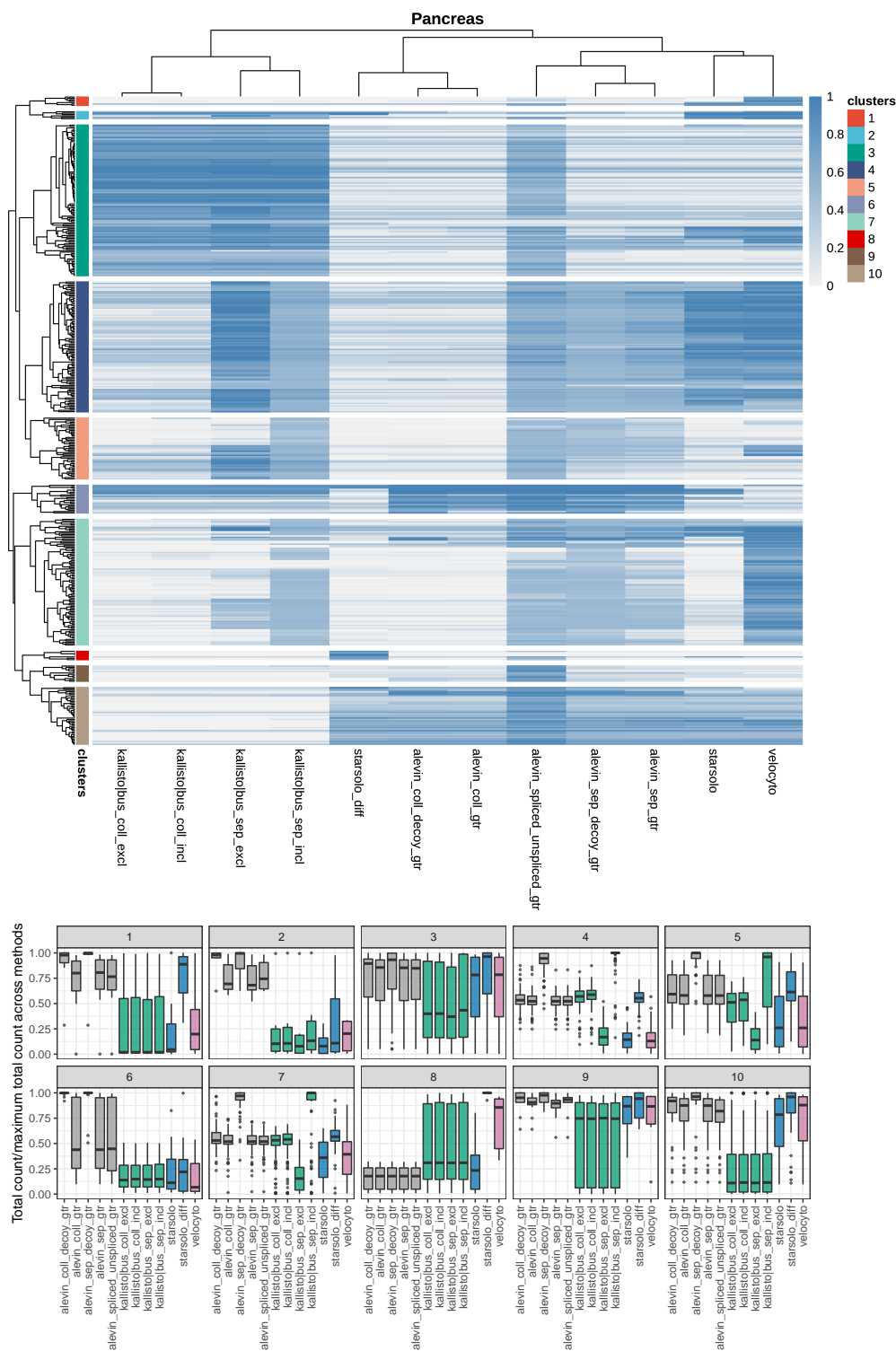


Figure 2: **Clustering of genes based on the fraction of unspliced counts.** Top panel: Heatmap showing the unspliced UMI count fraction, across all cells, in the Pancreas data. The dendrogram was cut into 10 clusters, indicated by colors to the left of the heatmap. Bottom panel: Relative total count assigned to each gene by the different methods, stratified by gene cluster.

409 of one gene can overlap either introns or exons of other genes, and the overlap can be on the same or
410 on opposite strands. Reads falling in an exon of one gene and in an intron of another gene on the same
411 strand are considered ambiguous, and are therefore discarded, by *kallisto|bustools*, *velocity* and *starsolo*.
412 In contrast, *alevin* does not discard the reads, but instead distributes them between the two features.
413 Thus, *alevin* tends to give a higher fraction of unspliced counts, and in many cases also a higher total
414 count, for genes with other genes in their introns (cluster 6, exemplified by *Cnot6* in Fig. S7). It is worth
415 observing that *alevin* will often also assign reads to the gene located within the intron (*Gm12191* in
416 Fig. S7, which is the gene in the intron of *Cnot6*). As for the previous category of genes, *alevin* with
417 the decoy approach double-counts reads mapping equally well to an exon and an intron, regardless of
418 whether or not the exon and the intron belong to the same gene.

419 In cases of exonic overlap between genes on the same strand (clusters 1 and 2, exemplified by *Chkb*
420 and *Gm21983* in Fig. S7), all methods except *alevin* consider the corresponding reads ambiguous and
421 discards them, leading to a large difference in the total counts (Fig. 2). The main difference between
422 clusters 1 and 2 is that in cluster 1, the gene of interest overlaps partly with an intron of the other gene,
423 and the reads in the overlapping region may be counted by the 'Gene' approach of *starsolo-diff*. In cluster
424 2, the gene of interest overlaps only with exons of the other gene in the region.

425 Reads falling in overlapping regions of genes *on opposite strands* are not considered ambiguous if the
426 strandedness of the reads is taken into account. However, not accounting for the strandedness (illustrated
427 here by the behaviour of *kallisto|bustools*) implies treating such overlaps similar to same-strand overlaps.
428 For example, for a gene located inside the intron of another gene on the opposite strand, all reads not
429 mapping across an exon-exon junction will map equally well to the two genes and thus be discarded
430 (cluster 10, exemplified by *Tmem120b* in Fig. S7). Exonic overlaps between genes on opposite strands
431 also leads to a decrease in the number of assigned reads if the strandedness is not taken into account
432 (exemplified by *Rassf1* in Fig. S7). The assigned count can also increase by performing the quantification
433 in an unstranded manner. For example, reads mapping to the negative strand, not overlapping any
434 feature there but overlapping a gene on the positive strand, can be assigned to the latter. Intronic reads
435 resulting from discordant priming from poly-T sequences, as observed by La Manno et al. (2018), would
436 also be incorporated with an strand-agnostic counting approach. The observation of La Manno et al.
437 (2018) could be reproduced in our data sets (Fig. S8), and the incorporation of opposite-strand reads by
438 *kallisto|bustools* is exemplified by *Ssr1* and *Brsk2* in Fig. S6.

439 **Genes with reads only partly overlapping the gene body** (cluster 8, exemplified by *1810019D21Rik*
440 in Fig. S6). In some cases, reads extend outside the annotated gene body. The *starsolo_diff* 'GeneFull'
441 count incorporates these reads, while the 'Gene' count from the same method does not, since they are
442 not compatible with the annotated gene model. As an effect, the difference between them (which is used
443 as the intronic count) can be high, even in cases where the gene does not contain introns, and the total
444 count assigned by *starsolo_diff* is higher than most of the other methods. *Velocity* and, for some genes in
445 the cluster, the *kallisto|bustools* methods, yield a high spliced count, while the *alevin* methods and *starsolo*
446 return lower values.

447 **Reads falling in purely exonic regions.** Across the clusters, *alevin_spliced_unspliced* often shows a
448 different read assignment compared to the other methods. As previously noted, there is a fundamental
449 difference between the reference used for *alevin_spliced_unspliced* (which considers full spliced and un-
450 spliced transcripts) and those used for the other methods (which consider transcripts and introns). This

451 implies that reads falling completely in exonic regions, from the point of view of *alevin_spliced_unspliced*,
452 are equally likely to come from a spliced as an unspliced molecule, while the other methods consider
453 such reads unambiguously exonic. In practice, this can lead to a lower exonic count and a more even
454 exonic/intronic count ratio for *alevin_spliced_unspliced* than for the other methods. This is exemplified by
455 Map1b (cluster 9) in Fig. S6.

456 **Large differences in inferred velocities between quantification methods**

457 In the previous sections we showed that there are noticeable differences between the quantification meth-
458 ods, in terms of the total number of UMI counts as well as the distribution of these between spliced and
459 unspliced targets. Next, we asked whether these differences could be seen also in the velocity estimates
460 from *scVelo*, and in the embedding of these in a low-dimensional representation of the cells, which is ar-
461 guably the most widely used way of interpreting RNA velocity estimates. For our analyses, we provided
462 *scVelo* with raw spliced and unspliced UMI count matrices. These were then filtered and normalized by
463 *scVelo*, and the RNA velocity was estimated for each input gene and each cell. Velocities were estimated
464 for either the individual sets of 2,000 highly variable genes from each quantification method, or the set
465 of genes that were selected by *scVelo* (and obtained a valid velocity value) with all the quantifications.

466 Interestingly, the estimated velocities consistently showed a lower correlation between methods than
467 the normalized (spliced, unspliced or aggregated) abundances, when calculated across either cells or
468 genes (Fig. S9). Within a cell, there was also a relatively strong correlation between the total gene abun-
469 dance and the absolute value of the velocity (Fig. S10). This should be factored in when comparing
470 absolute velocities across genes, and it may also suggest that velocity estimates are not directly compa-
471 rable across quantification methods if the number of assigned reads are very different. For a given gene,
472 the fraction of unspliced counts was also moderately positively correlated with the estimated velocity.
473 The spliced and unspliced abundances were positively correlated for all quantification methods, suggest-
474 ing that the intronic signal is indeed real and of potential biological relevance, rather than just the result
475 of, e.g., contamination by genomic DNA. Finally, we noticed a moderate positive correlation between the
476 abundance of a gene and the likelihood of the velocity fit in three of the four data sets (exemplified by
477 the Pancreas data set in Fig. S11), while it was substantially lower in the Dentate gyrus data set (Fig. S12).

478 The velocity estimates were visualized by embedding them into a UMAP representation based on
479 the *alevin_spliced* quantification (note that the *alevin_spliced* counts are not used to estimate the velocity,
480 since no intronic counts are estimated). The UMAP embedding was compared to other types of em-
481 beddings (PCA, tSNE, UMAP based on aggregated abundances, unspliced abundances only or spliced
482 and unspliced abundances concatenated), in terms of the length of the embedded velocity vectors as
483 well as the average distance between the velocity vector of each cell and its 10 nearest neighbors. These
484 comparisons suggested that the differences between embeddings were relatively minor, but that UMAP
485 often provided a slightly more interpretable representation (Figs. S13-S14). Embeddings based solely on
486 unspliced abundances were least interpretable from a velocity perspective.

487 **Differences in velocity estimates directly affect biological interpretation**

488 From the UMAP visualizations it is immediately apparent that the differences in the estimated abun-
489 dances between the quantification methods directly influence interpretation, e.g., indicated by stream-

490 lines pointing in different directions in certain regions of the plots (Figs. S15-S17). These differences are
491 not captured by the velocity confidence estimates returned by *scVelo* for an individual method, which are
492 often high for all the cells (Figs. S18-S20), suggesting that the differences between methods are systematic
493 rather than just the result of random fluctuations or uncertainty in the velocity estimation. The similarity
494 among the low-dimensional velocity embeddings based on different quantification methods increased
495 somewhat when they were derived from the set of shared genes (Fig. 3). However, considerable differ-
496 ences were still seen, indicating that the quantification does not only influence the velocity interpretation
497 via the selection of genes.

498 The lack of unambiguous ground truth complicates a direct evaluation of the accuracy of velocity
499 estimates from the different quantification methods. In addition, the typical way of interpreting velocity
500 estimates by means of embedded stream lines in a low-dimensional space provides a relatively coarse-
501 grained measure. Nevertheless, Figs. 3 and S15 suggest that for the Pancreas data, the largest differences
502 between methods appear in the differentiated Alpha, Beta, Delta and Epsilon cell types (top left). Here,
503 *alevin_sep_decoy_gtr* and the *kallisto|bus* methods induce (partly or fully) a 'back-flow', with streamline
504 arrows pointing from the differentiated cells back towards the pre-endocrine cells. A similar observation
505 can be made for *alevin_spliced_unspliced_gtr* and *kallisto|bus_sep_incl* for the pre-endocrine cells. The
506 cycling nature of the ductal cells is visible in the embeddings of velocities from most quantification
507 methods, with the exception of *alevin_spliced_unspliced_gtr*, *alevin_sep_decoy_gtr*, *kallisto|bus_coll_incl*, and
508 *kallisto|bus_sep_incl*.

509 Also for the spermatogenesis data (Figs. 3, S16), the largest differences between methods are seen to-
510 wards the end of the developmental trajectory. Again, many methods (with the exception of *alevin_sep_gtr*
511 and *kallisto|bus_sep_excl*) induce a back-flow, with streamline arrows pointing from the late round sper-
512 matids towards the mid round spermatid cluster. In most cases, this back-flow continues through (part
513 of) the mid round spermatid cluster as well.

514 In the dentate gyrus data, the lowest concordance between velocities based on different quantifica-
515 tions is seen for the cells in the granule cell lineage (middle part). While some quantifications indicate
516 a direction largely from neuroblasts to granule cells (e.g., *alevin_sep_gtr*, *kallisto|bus_coll_incl*), others in-
517 dicate a strong movement in the opposite direction (e.g., *alevin_sep_decoy_gtr*, *kallisto|bus_sep_incl*). All
518 methods except *kallisto|bus_coll_excl*, *kallisto|bus_sep_excl* and *kallisto|bus_coll_incl* show a strong dy-
519 namic flow within the mature granule cells, and there is further disagreement within the astrocyte cell
520 cluster. Overall, the results from these three data sets highlight that the biological interpretation can be
521 strongly affected by the choice of quantification method.

522 **Negative control data**

523 The PFC data set was used to compare the methods in terms of their performance on a 'negative control'
524 data set, that is, a data set where no strong systematic dynamics are expected. Here, we chose to compare
525 the methods in terms of the maximal cosine correlation between the estimated velocity vector for a cell
526 and the displacement vector to other nearby cells, as calculated by *scVelo*. A low value of this quantity
527 indicates that the velocity vector of a cell does not point in a direction compatible with the difference to
528 any neighboring cell in the data set, which is used here as a proxy for a lack of systematic dynamics.
529 While the maximal cosine correlation varied considerably among cell types (Fig. S21-S24), the value was
530 typically slightly lower for the PFC data set than for the data sets with known dynamics (Fig. 4). The

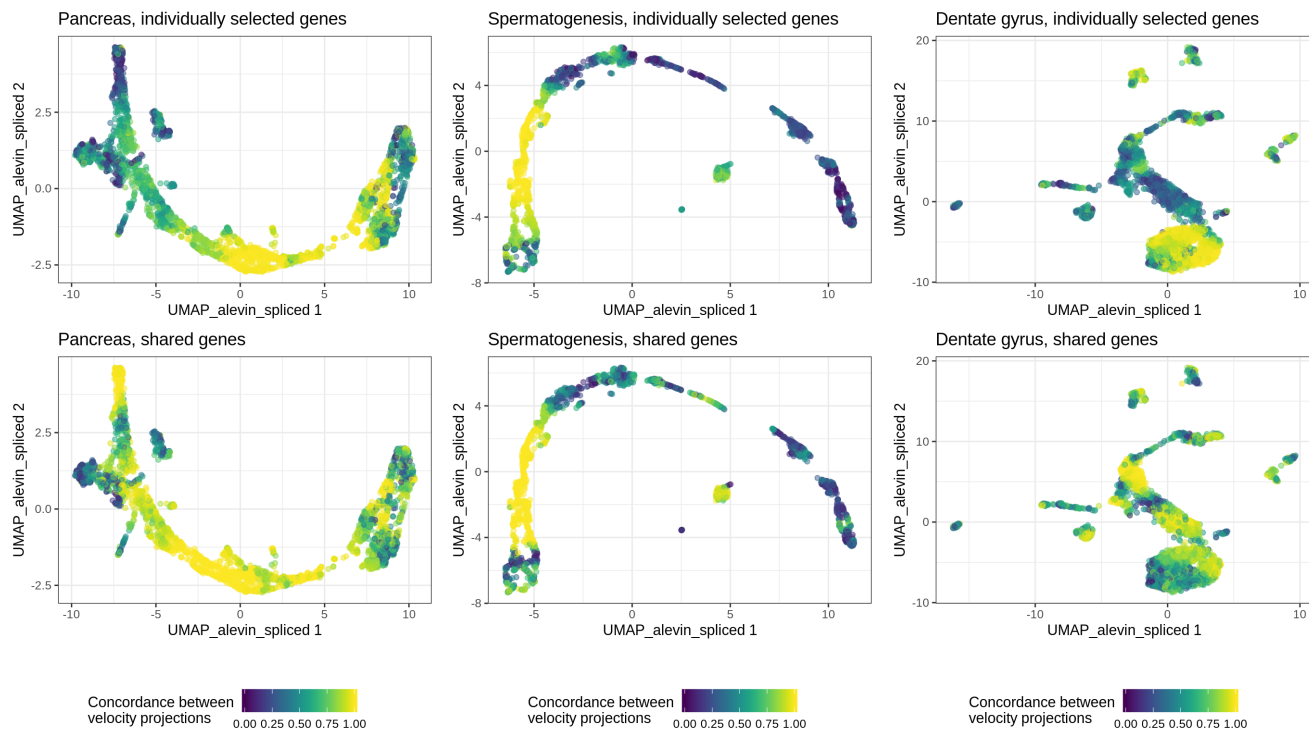


Figure 3: Concordance of velocity projections. Each panel colors the UMAP embedding of the cells by the concordance of velocity projections across methods for one of the three data sets expected to contain systematic dynamics. The concordance for a given cell was defined as the ratio between the length of the sum of the velocity embeddings for the different quantification methods, and the sum of the lengths of the same embedding vectors. A value close to 1 indicates that the embedded velocity vectors all point in the same direction, while a low value indicates larger deviations among them. For each data set, the top panel shows the concordance between the velocity embeddings derived based on all the 2,000 genes selected by *scVelo* for each method, while the bottom panel shows the concordance between the embeddings obtained when only the genes selected for all methods were considered (see also Fig. S5).

531 exceptions were *velocityto*, *alevin_sep_decoy_gtr* and *kallisto|bus_sep_incl*, for which the estimated velocities
532 often correlated strongly with the displacement vector to at least one other cell in the negative control
533 data set. We also estimated the standard deviation of the estimated latent times, within each cell type
534 (Fig. S25). In a data set with no continuous trajectories, we would expect a low variation within a cell
535 type (even if there are large differences between cell types). For all methods, the PFC data set indeed
536 showed the lowest variation, as expected.

537 Discussion and Conclusions

538 In this study, we have compared different counting strategies for obtaining the spliced and unspliced
539 count matrices required for RNA velocity analysis. Using four experimental droplet scRNA-seq data
540 sets, we have shown that there are considerable differences between the count matrices obtained by
541 different methods that are widely used in the field, and that these differences directly influence the
542 downstream analysis and interpretation of the estimated velocities. This effect is mediated partly by an

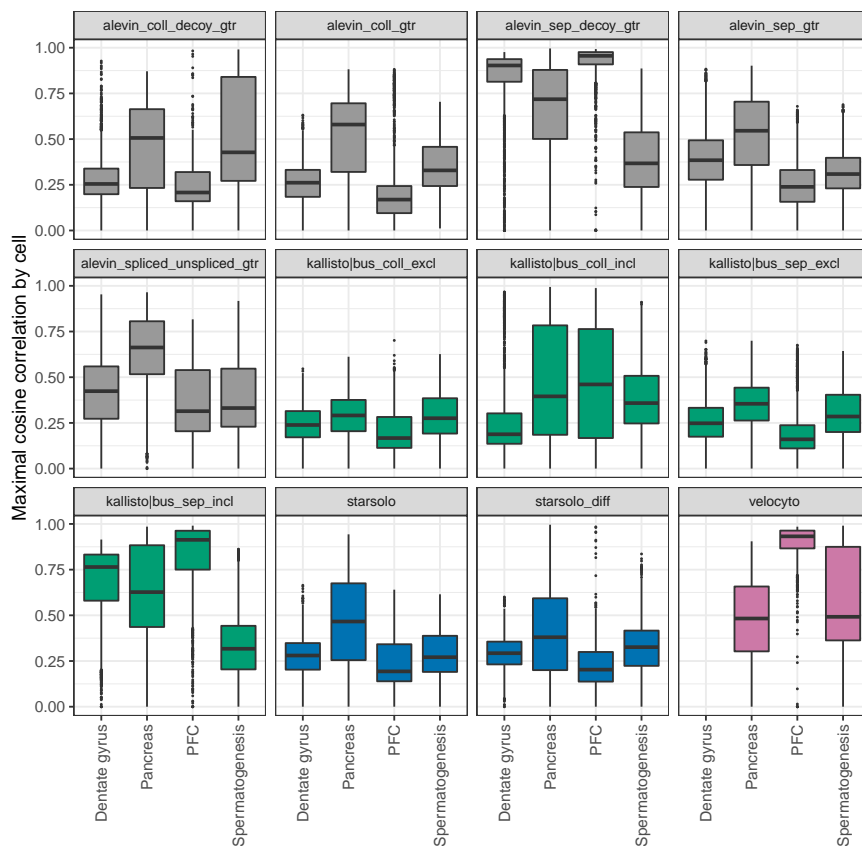


Figure 4: **Maximal cosine correlation.** The box plots show the distribution, across cells, of the maximal cosine correlation between the velocity vector and the displacement vector to other cells in the neighborhood, estimated by *scVelo* for different quantification methods in the four data sets.

543 impact on the genes that are selected for inclusion by *scVelo*, but differences affecting the interpretation
 544 remain even when the same set of genes is used across all methods.

545 Given the relative immaturity of the RNA velocity field, and the lack of a generally accepted method
 546 for generating realistic, simulated data with known ground truth for this application, it is challenging
 547 to rank the quantification methods in terms of absolute performance. However, some clear themes
 548 emerge from our analysis. First, counting exonic and intronic reads separately, without consideration
 549 of whether the read could have resulted from the other type of feature (exemplified here mainly by
 550 *alevin_sep_decoy_gtr* and *kallisto|bus_sep_incl*) leads to double-counting of reads, and velocities that agree
 551 less well with expectations. Second, not considering the strandedness of the reads from 10x Genomics
 552 (here exemplified by the *kallisto|bustools* variants and by explicitly running *alevin* in unstranded mode)
 553 implies that many reads in regions where genes on different strands overlap each other (exonically or
 554 intronically) are considered ambiguous. Depending on the method, these reads may consequently be
 555 excluded from the quantifications. However, at the same time it provides to ability to include reads
 556 resulting from discordant internal priming. Third, deriving the intronic reads by subtracting the 'Gene'
 557 count from *STARsolo* from the corresponding 'GeneFull' count (here denoted *starsolo_diff*) sometimes
 558 has unexpected consequences, since the 'GeneFull' counting considers all reads that overlap the gene
 559 locus, while the 'Gene' counting requires that the reads are consistent with the transcript model. Thus,

560 a gene can obtain a nonzero 'intronic' count despite completely lacking annotated introns. Moreover,
561 genes located within introns of other genes will often obtain a nominally negative intronic UMI count
562 since non-junction-spanning reads mapping to the former will be considered ambiguous and discarded
563 in the 'GeneFull' counting. Fourth, for 3' tag data such as the 10x Genomics data we have considered in
564 this study, quantifying the spliced and unspliced transcripts (rather than spliced transcripts and introns
565 only) implies that for a large fraction of the reads, it is difficult to resolve whether they stem from the
566 spliced or unspliced target. Thus, this type of reference may be more suitable for full-length scRNA-seq
567 protocols, where reads are sampled across the entire length of the transcript.

568 Among the counting strategies contrasted in this manuscript, *alevin_sep_gtr*, *kallisto | bus_sep_excl*, *star-*
569 *solo* and *alevin_coll_gtr* provided velocity embeddings most in line with expectations in the three real data
570 sets. However, even among these methods, there are large differences in the assigned counts as well as in
571 the handling of ambiguous reads and genomic regions. Going forward, we expect that improvements in
572 counting strategies for scRNA-seq data, specifically tailored for RNA velocity preprocessing, will likely
573 come alongside an increased understanding of the read generation process and the biases underlying
574 specific scRNA-seq library preparation protocols, and that different counting strategies may be optimal
575 for different types of scRNA-seq data. An increased understanding of the read generation process will
576 also enable realistic simulation of sets of spliced and unspliced scRNA-seq reads, which in turn will
577 provide an improved platform for objective evaluation of the performance of counting strategies.

578 Data and code access

579 The code used for our analyses is available on https://github.com/csoneson/rna_velocity_quant.
580 The spermatogenesis data can be downloaded from GEO, accession number GSE109033. The pancreas
581 data set was downloaded from GEO, accession number GSE132188. The dentate gyrus data set was
582 downloaded from GEO, accession number GSE95315. The PFC data set is accessible from GEO under
583 accession number GSE124952 (sample accession number GSM3559979).

584 Acknowledgements

585 The authors would like to thank Dania Machlab, Panagiotis Papasaikas and Michael I Love for helpful
586 discussions and comments on the manuscript.

587 Funding

588 This work has been supported by R01 HG009937, NSF CCF-1750472, and CNS-1763680 to R.P. The fun-
589 ders had no role in study design, data collection and analysis, decision to publish, or preparation of the
590 manuscript.

591 Disclosure declaration

592 RP is a co-founder of Ocean Genomics Inc.

593 References

- 594 Bastidas-Ponce, A. et al. (2019). “Comprehensive single cell mRNA profiling reveals a detailed roadmap
595 for pancreatic endocrinogenesis”. *Development* 146:dev173849.
- 596 Bergen, V., M. Lange, S. Peidli, F. A. Wolf, and F. J. Theis (2019). “Generalizing RNA velocity to transient
597 cell states through dynamical modeling”. *bioRxiv* doi:10.1101/820936.
- 598 Bhattacharjee, A., M. N. Djekidel, R. Chen, W. Chen, L. M. Tuesta, and Y. Zhang (2019). “Cell type-
599 specific transcriptional programs in mouse prefrontal cortex during adolescence and addiction”. *Nat.*
600 *Commun.* 10 (1), p. 4169.
- 601 Bray, N. L., H. Pimentel, P. Melsted, and L. Pachter (2016). “Near-optimal probabilistic RNA-seq quan-
602 tification”. *Nat. Biotechnol.* 34, p. 525.
- 603 Dobin, A., C. A. Davis, F. Schlesinger, J. Drenkow, C. Zaleski, S. Jha, P. Batut, M. Chaisson, and T. R.
604 Gingeras (2013). “STAR: ultrafast universal RNA-seq aligner”. *Bioinformatics* 29 (1), pp. 15–21.
- 605 Frankish, A. et al. (2019). “GENCODE reference annotation for the human and mouse genomes”. *Nucleic*
606 *Acids Res.* 47.D1, pp. D766–D773.
- 607 Gaidatzis, D., L. Burger, M. Florescu, and M. B. Stadler (2015). “Analysis of intronic and exonic reads
608 in RNA-seq data characterizes transcriptional and post-transcriptional regulation”. *Nat. Biotechnol.* 33
609 (7), pp. 722–729.
- 610 Gray, J. M. et al. (2014). “SnapShot-Seq: A method for extracting genome-wide, in Vivo mRNA dynamics
611 from a single total RNA sample”. *PLoS One* 9 (2), e89673.
- 612 Hahne, F. and R. Ivanek (2016). “Statistical Genomics: Methods and Protocols”. Ed. by E. Mathé and S.
613 Davis. New York, NY: Springer New York. Chap. Visualizing Genomic Data Using Gviz and Biocon-
614 ductor, pp. 335–351. ISBN: 978-1-4939-3578-9.
- 615 Hermann, B. P. et al. (2018). “The Mammalian Spermatogenesis Single-Cell Transcriptome, from Sper-
616 matogonial Stem Cells to Spermatids”. *Cell Rep.* 25 (6), 1650–1667.e8.
- 617 Hochgerner, H., A. Zeisel, P. Lönnerberg, and S. Linnarsson (2018). “Conserved properties of dentate
618 gyrus neurogenesis across postnatal development revealed by single-cell RNA sequencing”. *Nat. Neu-*
619 *rosci.* 21 (2), pp. 290–299.
- 620 Kent, W. J., A. S. Zweig, G Barber, A. S. Hinrichs, and D Karolchik (2010). “BigWig and BigBed: enabling
621 browsing of large distributed datasets.” *Bioinformatics* 26 (17), pp. 2204–2207.
- 622 La Manno, G. et al. (2018). “RNA velocity of single cells”. *Nature* 560, pp. 494–498.
- 623 Lawrence, M., W. Huber, H. Pagès, P. Aboyoun, M. Carlson, R. Gentleman, M. Morgan, and V. Carey
624 (2013). “Software for Computing and Annotating Genomic Ranges”. *PLoS Computational Biology* 9 (8).
- 625 Lun, A. and D. Risso (2019). *SingleCellExperiment: S4 Classes for Single Cell Data*. R package version 1.8.0.
- 626 McCarthy, D. J., K. R. Campbell, A. T. L. Lun, and Q. F. Wills (2017). “Scater: pre-processing, quality
627 control, normalization and visualization of single-cell RNA-seq data in R”. *Bioinformatics*, btw777.
- 628 McInnes, L., J. Healy, and J. Melville (2018). “UMAP: Uniform Manifold Approximation and Projection
629 for Dimension Reduction”. arXiv: 1802.03426 [stat.ML].
- 630 Melsted, P., V. Ntranos, and L. Pachter (2019). “The Barcode, UMI, Set format and BUStools”. *Bioinfor-*
631 *matics* 35 (21), pp. 4472–4473.
- 632 Melsted, P., A. S. Boeshaghi, F. Gao, E. da Veiga Beltrame, L. Lu, K. E. Hjorleifsson, J. Gehring, and L.
633 Pachter (2019). “Modular and efficient pre-processing of single-cell RNA-seq”. *bioRxiv* doi:10.1101/673285.
- 634 Moses, L. and L. Pachter (2019). *BUSpaRse: kallisto | bustools R utilities*. R package version 1.0.0.

- 635 Pagès, H. (2019). *BSgenome: Software infrastructure for efficient representation of full genomes and their SNPs*.
636 R package version 1.54.0.
- 637 Patro, R., G. Duggal, M. I. Love, R. A. Irizarry, and C. Kingsford (2017). “Salmon provides fast and
638 bias-aware quantification of transcript expression”. *Nat. Methods* 14 (4), pp. 417–419.
- 639 Quinlan, A. R. and I. M. Hall (2010). “BEDTools: a flexible suite of utilities for comparing genomic
640 features.” *Bioinformatics* 26 (6), pp. 841–842.
- 641 Saelens, W., R. Cannoodt, H. Todorov, and Y. Saeys (2019). “A comparison of single-cell trajectory infer-
642 ence methods”. *Nat. Biotechnol.* 37, pp. 547–554.
- 643 Srivastava, A., L. Malik, T. Smith, I. Sudbery, and R. Patro (2019a). “Alevin efficiently estimates accurate
644 gene abundances from dscRNA-seq data”. *Genome Biol.* 20 (1), p. 65.
- 645 Srivastava, A., L. Malik, M. Zakeri, H. Sarkar, C. Sonesson, M. I. Love, C. Kingsford, and R. Patro
646 (2019b). “Alignment and mapping methodology influence transcript abundance estimation”. *bioRxiv*
647 doi:10.1101/657874.
- 648 Wolf, F. A., P. Angerer, and F. J. Theis (2018). “SCANPY: large-scale single-cell gene expression data
649 analysis”. *Genome Biol.* 19 (1), p. 15.
- 650 Zeisel, A. et al. (2011). “Coupled pre-mRNA and mRNA dynamics unveil operational strategies under-
651 lying transcriptional responses to stimuli”. *Mol. Syst. Biol.* 7, p. 529.
- 652 Zheng, G. X. Y. et al. (2017). “Massively parallel digital transcriptional profiling of single cells”. *Nat.*
653 *Commun.* 8, p. 14049.